Smart Mn^{7+} Sensing via Quenching on Dual Fluorescence of Eu^{3+} Complex-Modified TiO_2 Nanoparticles

Wenbin Yang [a], Siqi Niu [a], Yao Wang [a], Linjun Huang [a], Shichao Wang [a], Ketul C. Popat [c,d,], Matt J. Kipper [b,d], Laurence A. Belfiore [b], Jianguo Tang [a,*]*

[a] Institute of Hybrid Materials, National Center of International Joint Research for Hybrid Materials Technology, National Base of International Sci. & Tech. Cooperation on Hybrid Materials, Qingdao University, 308 Ningxia Road, Qingdao 266071, P. R. China

[b] Department of Chemical and Biological Engineering, Colorado State University, Fort Collins, Colorado 80523, USA

[c] Department of Mechanical Engineering, Colorado State University, Fort Collins, Colorado 80523, USA

[d] School of Biomedical Engineering/School of Advanced Materials Discovery, Colorado State University, Fort Collins Colorado 80523, USA

*Corresponding author e-mail addresses: tang@qdu.edu.cn (Jianguo Tang), ketul.popat@colostate.edu (Ketul C. Popat)

Abstract

In this work, titania (TiO_2) nanoparticles modified by $Eu(TTA)_3Phen$ (ETP) were prepared by a simple solvothermal method to set up an easy Mn^{7+} pollutant sensing system. The characterization results indicate that the ETP causes structural deformation and the redshifts of UV-visible light absorptions of host TiO_2 nanoparticles. The ETP also reduces the crystallinity and crystallite size of TiO_2 nanoparticles. Compared with TiO_2 nanoparticles modified by Eu^{3+}, TiO_2 nanoparticles modified with ETP (TiO_2-ETP) exhibit significantly stronger photoluminescence under the excitation of 394 nm. Under UV excitation, TiO_2-ETP nanoparticles showed blue and red emission corresponding to TiO_2 and Eu^{3+}. In addition, as the concentration of ETP in TiO_2 nanoparticles increases, the PL intensity at 612 nm also increases. When ETP-modified TiO_2 nanoparticles are added to an aqueous solution containing Mn^{7+}, the fluorescence intensity of TiO_2 and ETP decreases. The evolution of the fluorescence intensity ratio (I_1 / I_2) of TiO_2 and ETP is linearly related to the concentration of Mn^{7+}. The sensitivity of fluorescence intensity to Mn^{7+} concentration enables the design of dual fluorescence ratio solid particle sensors. The method proposed in here is simple, accurate, efficient, and not affected by the environmental conditions.

KEYWORDS: TiO_2 nanoparticle; $Eu(TTA)_3Phen$; Fluorescence sensor;Mn^{7+}; Eu^{3+}

1. Introduction

Manganese has two primary valence and oxidation states, namely Mn^{2+} and Mn^{7+}, which have different effects in practice [1, 2]. Mn^{7+} has widely been used as strong disinfectant, but its strong oxidation property and its heavy metal characteristic make it be a toxic and carcinogen species in water recycle system and human health[3]. In industry, Mn^{7+} has been used as strong oxidation agents to generate huge amount of toxic waste water [4]. The excessive manganese ions have made serious pollution to cause toxic drinking water and to damage to plants[5]. Thus, Mn^{7+} has attracted a lot of attention among the pollutants in recent years. Therefore, the detection of Mn^{7+} is very important for environment. Ion chromatography (IC) [6], atomic absorption spectrum (AAS) [7], inductively coupled plasma mass spectrum (ICP-MS) [8] and spectrophotometry [9] can be used to detect Mn^{7+}. Monitoring Mn^{7+} in water samples requires susceptible methods such as atomic spectrometry. However, due to the low efficiency of this method and the interference of impurities generated in the actual samples, it is generally complicated to directly detect the content of Mn^{7+} at low concentrations and it requires complicated pretreatment steps [10]. Therefore, it is necessary to explore a simple, accurate, efficient and anti-interference method to detect the content of Mn^{7+}.

Even with the use of highly sensitive metal ion detectors, the content level of Mn^{7+} in environmental samples is usually low or close to the detection limit, so the samples need a unique separation. When high concentrations of interfering particles are present in the matrix, efficient extraction of Mn^{7+} is required. Qian et al. proposed a FAAS method that uses cross-linked chitosan to separate Mn^{2+} and Mn^{7+}. This method is simple and sensitive and can be used for environmental sample detection [11]. A potential problem to apply this method for actual samples is that the Mn^{2+} is determined by its oxidation to Mn^{7+}, and then the total Mn concentration is determined. Therefore, this method need that the testing species are only Mn^{2+} and Mn^{7+}. Based on this situation, the new method to be developed is necessary. Europium complexes constitute an important class of optical probes, with applications ranging from sensing of bioactive species, high throughput assays and screening protocols in vitro, to time-resolved imaging studies in cellulo or in vivo[12]. This provides a possible chance for Mn^{7+} sensing. So, it becomes possible that we design a strategy to combine both the advantages of Eu^{3+} fluorescence property and TiO_2 dispersion in water medium in this work. Our fluorescent nanomaterials can sense in water or other liquids, with strong anti-interference ability and low cost. In recent years, fluorescence spectrometry has been used to determine metal ions[13]. A new method for the determination of copper, manganese, nickel, and lead in diesel oil has been developed, which combines liquid-liquid reversed-phase eddy microextraction and energy dispersive X-ray fluorescence spectroscopy [14]. Fluorescence sensors [15] have received widespread attention due to their high sensitivity, selectivity, and simple operation, however, a single wavelength fluorescence sensor is still affected by sample concentration, environmental factors, and

excitation intensity [16]. Dual fluorescence sensors can measure emission peaks at two different wavelengths, and make the ratio of the two peak intensities to achieve the purpose of solving the above problems [17-20], increasing sensitivity and selectivity by comparison [21, 22]. Nanomaterial fluorescence sensors are new type of sensors, which have large specific surface area, strong encapsulation ability, controllable aperture, predictable nanostructure[23-25], polychromatic and adjustable radiation characteristics [26]. In general, photoluminescence with lanthanide ions as the center, UV excitation and lanthanide ions will form an f-f or f-d energy transfer system [27, 28]. Among all the lanthanide ions, europium ions have been widely used because of their prominent emission peak and long fluorescence lifetime [29-31]. The advantages of their complexes are stable characteristic emission peaks and increased fluorescence intensity. TiO_2 nanoparticles have excellent optical properties, catalytic properties, chemical stability, and biocompatibility [32]. Therefore, TiO_2-ETP nanoparticles combine the advantages and fluorescence properties of europium complexes and TiO_2 nanoparticles.

In this work, we synthesized Europium complex-modified TiO_2 nanoparticles (TiO_2-ETP) by a solvothermal method, and further the structure, properties, and applications of TiO_2-ETP nanoparticles were investigated. The resulting nanoparticles have outstanding luminescence characteristics, which indicates the possibility of using TiO_2 nanoparticles to improve the effective luminescent materials of rare earth complexes. TiO_2-ETP nanoparticles exhibit significantly stronger photoluminescence (PL) than TiO_2- Eu^{3+} nanoparticles. Thus, TiO_2-ETP nanoparticles have the potential to be used as new semiconductor luminescent materials. In our study, the fluorescence intensity of TiO_2-ETP was sensitive to the change of Mn^{7+} concentration. In addition, the high specific surface area of TiO_2 nanoparticles can increase the contact area between the sensor and Mn^{7+}, which can improve the sensitivity of the sensor. In the fluorescence spectrum, excited with an excitation wavelength of 394 nm, TiO_2-ETP has emission peaks at 454 nm and 616 nm, respectively. The fluorescence of TiO_2 and ETP will decrease by Mn^{7+} and the characteristic emission will not change after the addition of Mn^{7+}. The Mn^{7+} dual fluorescence sensor shows a wide detection range and high sensitivity, and the effectiveness of the sensor has been verified through experiments. In this research, we propose an intelligent dual fluorescence sensor, which is low-cost, easy to operate. It has high sensitivity and high efficiency. Compared with previous reports[33, 34], our method is simple and practical, non-pretreatment, and has a larger detection range. The preparation and detection mechanism of the sensor is shown in Fig. 1.

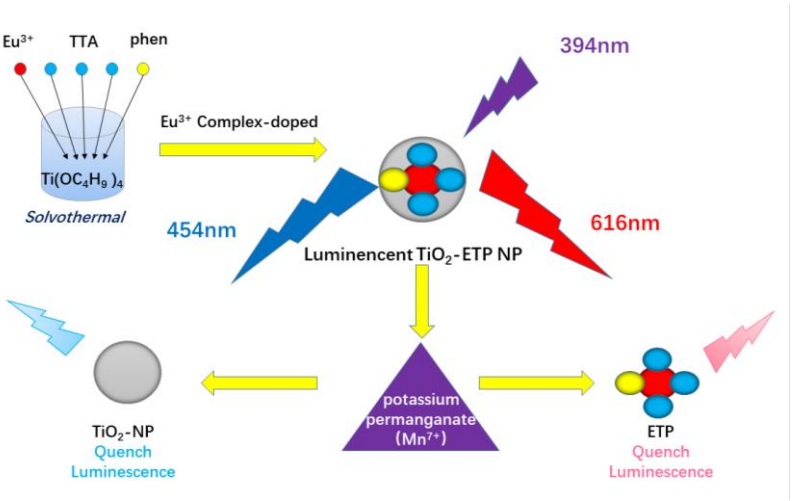


Fig. 1. Schematic illustration of TiO_2 nanoparticles modified with $Eu(TTA)_3Phen$ preparation and sensing mechanism of manganese concentration.

2. Experimental details

Ethanol (AR,99.7%), acetic acid (AR,99.7%), and Tetrabutyl titanate (AR) were purchased from Macklin. Europium chloride hexahydrate ($EuCl_3 \cdot 6H_2O$, 99.9%), 1,10-Phenanthroline Monohydrate (AR,98%) and 2-thenoyltrifluoroacetone (TTA,98%) were purchased from Aladdin.

In Fig. 2, TiO_2, TiO_2 modified with Eu^{3+} (TiO_2-Eu^{3+}), and TiO_2 modified with Eu $(TTA)_3Phen$ (ETP) (TiO_2-ETP) were prepared using the solvothermal method. Tetrabutyl titanate (TBT) was used as a precursor. Ethanol (CH_3CH_2OH) and acetic acid (CH_3COOH) was used as solvents and hydrolysis inhibitors. Before the final synthesis, two solutions were prepared (solution A and solution B). Solution A was prepared by adding acetic acid and TBT in ethanol. In solution B, dissolve the $EuCl_3$ in ethanol and stir for a while. To this mixture were added 1,10-phenanthroline monohydrate and methyl 1H-benzotriazole, dissolved in absolute ethanol. Stir the mixed solution with a magnetic stirrer for 1 hour at room temperature. Add Solution A to Solution B. The mixture became cloudy with continuous stirring. The mixture was added to the autoclave at 150°C for 24 hours. After the reaction, the resulting material was cooled to room temperature. The synthesized material was centrifuged and washed with ethanol and distilled water several times to remove impurities, and the white solid was collected and dried in an oven at 60°C. For the synthesis of unmodified TiO_2 nanoparticles, the same conditions are used. The difference is that no ETP is added.

The quenching experiments of metal ions were done by the mixture of TiO_2-ETP suspension and candidate metal ion solutions. TiO_2-ETP(0.1mol/L) was added into different testing metal ion solutions with the concentration of 1mM/L, and the mixtures were stirred for 2 hours. Whereas, to sense the quenching behavior, Mn^{7+} concentration was set in the range of 1μM/L to 1000μM/L gradiently.

Formatted: Font: Times New Roman

Formatted: Font: Times New Roman, Subscript

Formatted: Font: Times New Roman

Deleted: (TTA)Methyl-1H-benzotriazole

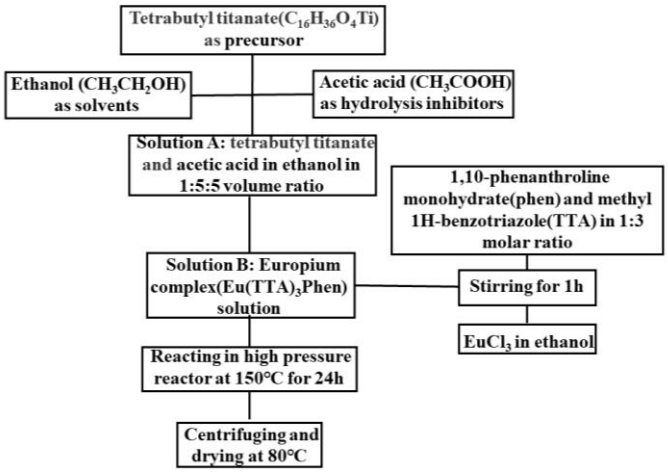


Fig. 2. Flow chart of experiment

A Thermo Scientific F200i (USA) transmission electron microscope was used to obtain transmission electron microscope (TEM) images at an accelerating voltage of 200 kV. X-ray powder diffraction (XRD) measurements were performed using a Bruker D8 Advance diffractometer (Germany), which was operated at a generator voltage of 40 keV and a current of 30 mA. The X-ray source is CuKα radiation (λ = 0.154 nm). The diffraction pattern was collected at a scanning speed of 1°/min within a 2θ scanning range of 20° to 80°. Measurements of Raman spectra were performed on a Thermo Scientific DXR 2xi (America) Raman Spectrometer under a backscattering geometry. The valence states of Eu, O, and Ti atoms were measured by X-ray photoelectron spectroscopy (XPS) on a Thermo Scientific ESCALAB 250 (USA) spectrometer. The XPS experiment was performed under vacuum using AlKα (1486.6 eV) radiation. The ultraviolet absorption spectrum was obtained using PerkinElmer Lambda 750s (USA) with solid sample frame, on which the powder samples were flattened when the powder samples were used. The PL spectrum is an important tool for determining the luminescent properties of materials. Edinburgh Instrument FLS 1000 (UK) was used to record the excitation and emission spectra of each sample, on which the data of excitation spectra, emission spectra, fluorescence lifetimes were collected. The excitation spectra and emission spectra of TiO_2 nanoparticles were recorded using the Edinburgh Fluorescence Spectrophotometer FLS 1000 (UK). A 450W xenon arc lamp capable of emitting a continuous spectrum with greater intensity was used as the light source. The excitation monochromator was used to select the specified excitation spectrum with the excitation wavelength of 394 nm. Fluorescence analyzer calibration is a work of high precision requirements, we were in accordance with the instrument operating procedures for rigorous standard sample, sample preparation and processing. Judging from the calibration curve, the expected ideal state is achieved.

3. Results and Discussion

3.1 Morphological structures

The additions of Eu^{3+} and ETP into TiO_2 change the shape and size of TiO_2 nanoparticles. Fig. 3 shows typical transmission electron microscopy (TEM) images of TiO_2 nanoparticles. TiO_2 nanoparticles with spherical morphology can be seen in TEM images (Fig. 3(a)). The morphology of TiO_2 nanoparticles with Eu^{3+} varies from spherical to ellipsoidal shapes (Fig. 3(b)). The TiO_2 nanoparticles modified with ETP has a cuboid shape (Fig. 3(c)). These changes are similar to the previous report[35]. Eu^{3+}- and ETP-doped TiO_2 cause different shapes of TiO_2- Eu^{3+} and TiO_2-ETP nanoparticles[36]. The corresponding histograms of the diameter distributions and the changes of the average sizes are shown in Fig. 3, in which the average nanoparticle sizes can be found to be 15 ± 0.09 nm, 12.3 ± 0.08 nm, and 9 ± 0.1 nm in diameter. The length of TiO_2-Eu^{3+} is between 10 and 40 nm. Compared to TiO_2, the average size of TiO_2-ETP nanoparticles decreases, which suggests that the inclusion of ETP largely suppresses the growth of TiO_2 nanoparticles. This size change of TiO_2-Eu^{3+} and TiO_2-ETP nanoparticles can also relate to crystalline structures described later based on X-ray diffraction analyses [37]. The growth of TiO_2 - Eu^{3+}crystals is hindered by the formation of Eu-O-Ti bond in the crystal void of TiO_2-Eu^{3+} nanoparticles. The decrease of particle size of ETP-modified TiO_2 is mainly caused by ETP entering the lattice and binding with oxygen vacancy. Due to their internal stress in the crystal lattice, the diffusion of Ti^{4+} and O^{2-} and the obstacle of crystal migration, they are not easy to produce crystal growth boundary [38].

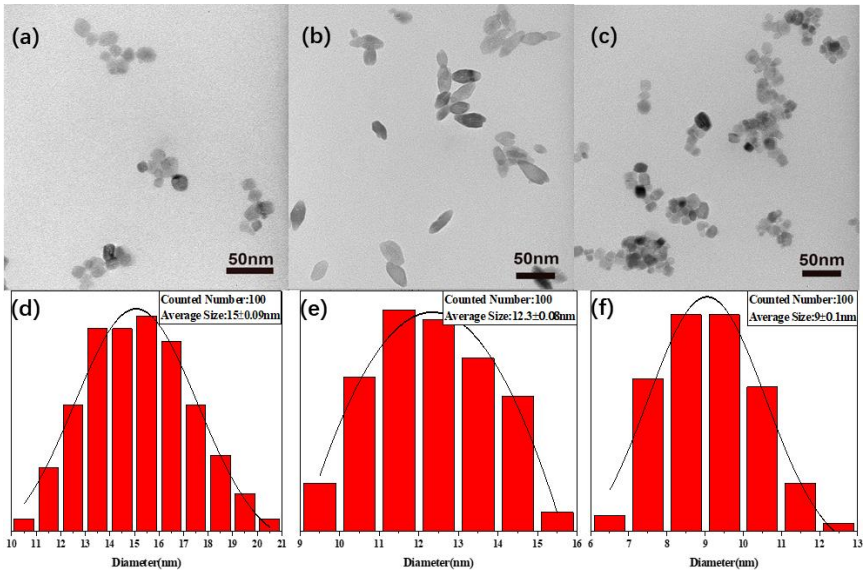


Fig. 3. TEM images of (a) TiO_2 (b) TiO_2-Eu^{3+} (c) TiO_2-ETP and diameter distribution histograms of (d) TiO_2 (e) TiO_2-Eu^{3+} (f) TiO_2-ETP

3.2 Crystalline structure

Modification with Eu^{3+} can effectively change the crystal structure and inhibit grain growth of TiO_2 nanoparticles. This effect is more pronounced when an organic complex (ETP) is used as a precursor. Fig. 4 shows the diffraction patterns of TiO_2 nanoparticles obtained by the solvothermal method. The presence of diffraction peaks corresponding to planes (101), (004), (200), (105), (211), and (204) indicates the formation of the anatase TiO_2 phase [39]. The XRD chart shows that TiO_2: Eu^{3+} and TiO_2-ETP nanoparticles have peaks at 2θ = 25.3 °, 38.1 °, 47.9 °, 54.1 °, 55.2 and 62.6 °, which correspond to peaks of anatase TiO_2 (JCPDS NO.21-1272)). No additional peaks of any other phases or impurities were found, which indicates the high purity of the nanoparticles. Fig. 4 shows that the XRD peaks of the crystal plane (101) in TiO_2-ETP are slightly shifted towards a smaller diffraction angle from 25.3 to 25.1, while other diffraction peaks almost have no observable shift. This is likely due to the addition of ETP [40]. Because the smaller diffraction angle relates to the larger gaps between crystal planes, this shift means that the distance of crystal plane (101) slightly increases, which are caused by added ETP [40]. The relative intensity of the peak at 2θ = 25.3 ° significantly decreased in TiO_2-ETP than TiO_2 and TiO_2-Eu^{3+} nanoparticles. The intensity of diffraction peak decreased obviously, indicating that the crystallinity decreased [41]. When ETP is modified on the surface of TiO_2 nanoparticles, deformation is induced in the system, leading to a change in the periodicity of the lattice and a decrease in the crystal symmetry. From the full width at half maximum, one can judge that TiO_2-ETP has a smaller particle size than TiO_2 and TiO_2-Eu^{3+}. Select the characteristic peak of the (101) (004) (200) crystal plane from the XRD image, and use the Scherrer formula (Equation 1) to calculate the average size of the modified and unmodified nanoparticles (Table 1).

$$L_{hkl} = \frac{K\lambda}{\beta cos\theta} \qquad (1)$$

Where "L_{hkl}" is the size of the particle crystallites, k is the shape constant, usually taken as 0.9, λ is the wavelength of X-rays (CuKα is 1.5406Å), β is the full diffraction width at half maximum, measured in radians at 2θ Peak.

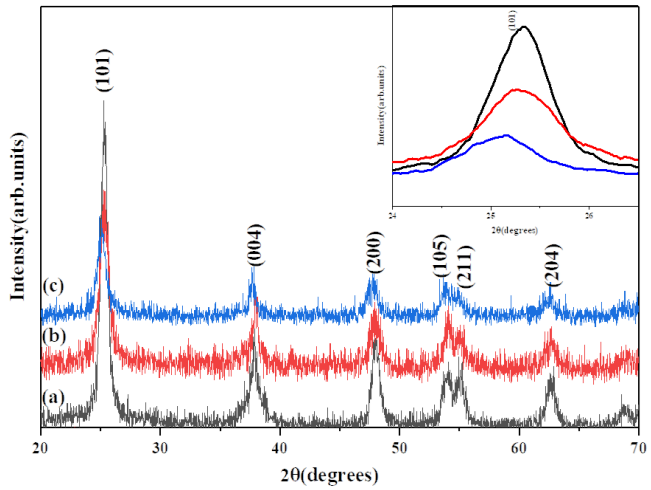


Fig. 4. XRD patterns for (a) TiO_2 (b) TiO_2-Eu^{3+} (c) TiO_2-ETP

Table 1. XRD results with parameters

Sample	hkl	2θ(deg)	D(Å)	FWHM(deg)	Mean grain size(nm)	Crystal structure
TiO_2	101	25.34	3.51	0.671	15.1	tetragonal
	004	37.84	2.37	0.846	15.0	tetragonal
	200	48.07	1.89	0.710	15.1	tetragonal
TiO_2-Eu^{3+}	101	25.31	3.50	1.115	12.2	tetragonal
	004	37.66	2.38	0.786	12.4	tetragonal
	200	47.88	1.89	0.825	12.1	tetragonal
TiO_2-ETP	101	25.06	3.55	0.966	9.0	tetragonal
	004	37.48	2.39	0.847	9.1	tetragonal
	200	47.76	1.90	0.971	8.9	tetragonal

Fig. 5 shows the Raman spectrum of the obtained TiO_2 nanoparticles. The Raman peaks at 143, 395, 514, and 639 cm^{-1} correspond to E_g, B_{1g}, A_{1g}, or B_{1g}, and E_g of the anatase phase, respectively [42]. The most vital E_g mode that appears due to the external vibration of the anatase structure is most apparent at 143 cm^{-1}. It indicates that the anatase phase is formed in the prepared europium complex-modified TiO_2 nanoparticles. TiO_2-ETP nanoparticles changed part of the crystal structure of TiO_2 due to the modified with ETP, so the Raman spectrum was slightly shifted. It can be seen from the Raman spectrum that, especially in the E_g mode near 144 cm^{-1}, the TiO_2 nanoparticles modified with ETP move to a higher wavenumber direction, and their intensity drops sharply. The observation can be explained by a decrease in the particle size in TiO_2-Eu^{3+} [41, 43, 44]. When the grain size decreases, it will significantly affect the Raman spectrum of titanium dioxide nanoparticles. Generally speaking, dimensional changes will produce pressure, and volume shrinkage will occur in TiO_2

nanoparticles. The reason for the increase in pressure is the decrease in the distance between atoms. The sudden drop in the intensity of the Raman spectrum, especially the drop in the scattering intensity of the E_g mode, is related to the destruction of the atomic symmetry of the crystal, which is caused by the defects modified with ETP. Because TiO_2-ETP nanoparticles have local lattice defects, the Raman peak becomes weaker and broader, which means that the crystallinity of synthesized nanoparticles decreases.

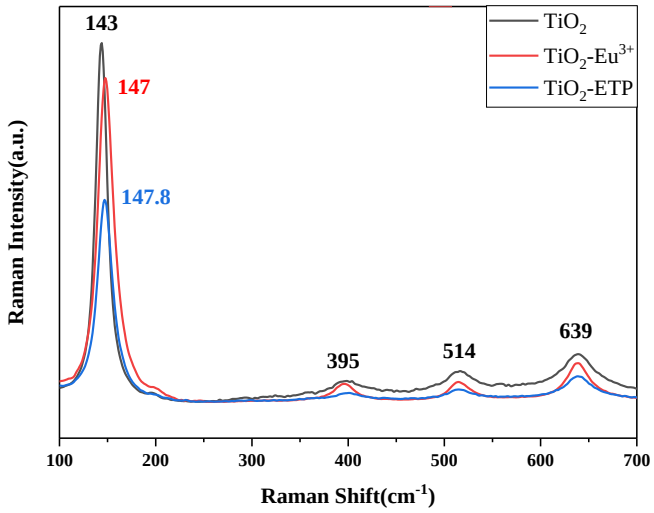


Fig. 5. Raman spectra of TiO_2, TiO_2-Eu^{3+} and TiO_2-ETP

3.5 Confirmation of Eu^{3+} in TiO_2

X-ray photoelectron spectroscopy (XPS) was used for elemental analysis of ETP-modified titanium dioxide nanoparticles. Fig. 6A(a, b, c) show the overview XPS spectra of TiO_2, TiO_2-Eu^{3+}, and TiO_2-ETP, respectively. The XPS spectra in Fig. 6(B) clearly shows the changes of binding energy spectra of Ti2p electron orbital in TiO_2, TiO_2-Eu^{3+}, and TiO_2-ETP, in which the binding energies in TiO_2, TiO_2-Eu^{3+} and TiO_2-ETP are gradually smaller at 458.72, 458.62, and 458.57 ev. This phenomenon is roughly similar to previous report [45],. The binding energy decreases are obviously caused by Eu^{3+} and ETP inserts between crystal planes, and the much obvious decrease of binding energy in TiO_2-ETP is due to the Eu^{3+}-carried ligands of TTA and Phen that have bigger sizes than that of Eu^{3+}. Fig. 6(C) of spectra of Eu3d show significantly higher intensity of TiO_2-ETP than that of TiO_2-Eu^{3+} that means Eu3d electron orbital has stronger binding state in TiO_2-ETP, which can be thought as the contribution of ligands of TTA and Phen. At the same time, the binding energy of Eu3d in TiO_2-ETP is much lower than that in TiO_2-Eu^{3+} that is also due to the stronger interaction of ligands with Eu3d electron orbital [46]. Fig. 6(D， E and F) show the binding energy changes of O1s in TiO_2, TiO_2-Eu^{3+}, and TiO_2-ETP, from which we can find that Ti-O and Eu-O have almost the same binding energies in TiO_2-$Eu^{3+}$and TiO_2-ETP, while the binding energy of Ti-O in TiO_2 is higher, which also indicates the influence of Eu^{3+}

insert between crystal planes of TiO_2. The binding energies corresponding to Ti-O, O-H, Eu-O and C=O in TiO_2-ETP(Fig. 6 (F) locate at 529.8, 530.8, 531.4, and 532.3 eV. Compared to TiO_2, the formation of an Eu-O bond indicates that Eu has reacted with TiO_2. The C=O bond belongs to TTA in ETP, which indicate that ETP is interacted with TiO_2[47-49].

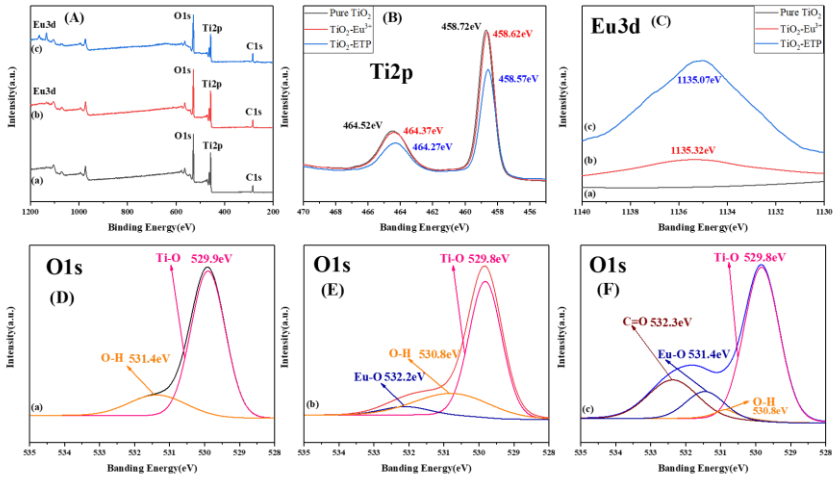


Fig. 6. (A) overview XPS spectra, (B)XPS spectra of Ti2p, (C) XPS spectra of Eu3d, (D,E,F) XPS spectra of O1s

Commented [THMC1]: Eu3+ 和 ETP 的含量

3.4 UV absorption and bandgap of TiO_2

Fig. 7(a and c) show the UV-visible absorption curves of TiO_2-Eu^{3+} and TiO_2-ETP. Compared with the curves of TiO_2-Eu^{3+} (Fig. 7(a)), the curves of TiO_2-ETP have significant redshift（Fig. 7(c)）. As the ETP concentration increases, the absorption edge moves to the right, and the energy required to generate electron-hole pairs gradually decreases. The valence band of TiO_2 absorbs ultraviolet light and releases it into the conduction band and defect state energy level of TiO_2. Due to the excited state of Eu^{3+} is lower than the conduction band and defect state, the energy is transferred to Eu^{3+} [50]. UV-visible spectra shown in Fig. 7 (b) show that modification with ETP shifted the TiO_2 absorption edge from the UV to the visible region. This means Eu^{3+} and ETP doping produce the defects in TiO_2 host crystal, and thus these defects result in band gap decrease [51-53].

The absorption spectra in the UV and visible regions of TiO_2-Eu^{3+} and TiO_2-ETP nanoparticles are used to estimate the bandgap. $[F(R) \times h\nu]^{1/2}$ of hν in the vicinity of the absorption edge are plotted for all samples in Fig. 7 (c, d). Where F(R) is the Kubelka-Munk function, defined as $F(R)=(1-R)^2 / 2R$, hν is the photon energy, and R is the reflection coefficient converted to absorption intensity. By extrapolating the linear part of the curve to the intersection with the x-axis, the bandgap energies can be estimated: 3.08 eV, 3.05 eV, 3.06, and 3.09 eV for TiO_2 modified by 2, 4, 6, and 8 mol%

Eu^{3+}. Indeed, these are 2.72 eV, 2.40 eV, 2.30 eV, and 2.26 eV for TiO_2 modified by 2, 4, 6, and 8 mol% ETP. Compared with the band gap 3.2 ev of TiO_2, the band gaps of TiO_2-Eu^{3+} and TiO_2-ETP decreased. Then, the proper reasons should be the interactions between TiO_2 host and dopants, either Eu^{3+} or ETP in TiO_2-Eu^{3+} and TiO_2-ETP respectively. Based on the results of XRD to indicate the crystal plane distance extension of (101) and that of XPS to confirm the interactions between Eu^{3+}-O and the binding energy changes of Eu3d and Ti2p in Eu_{3+} and ETP, we suppose that Eu^{3+} and ETP as dopants have interacted with TiO_2 with different ways. Thus, the understanding for this difference, can attribute to the "solubility limit" of Eu^{3+} and ETP in TiO_2 host. The former Eu^{3+} is from $EuCl_3 \cdot 6H_2O$, in which both the counter ion Cl^{1-} and the bringing H_2O molecules are typical polar species and affect the solubility of Eu^{3+}. However, ETP is a complex with rich organic ligand molecules of 1,10-phenanthroline (Phen) and 2-thenoyltrifluoroacetone (TTA), the organic ligands modified the solubility of ETP. Solubilized ions have efficient interaction with TiO_2 host to change the electron transition bandgap[54]. Also, the influences affect the fluorescence behaviors as shown in Fig. 8.

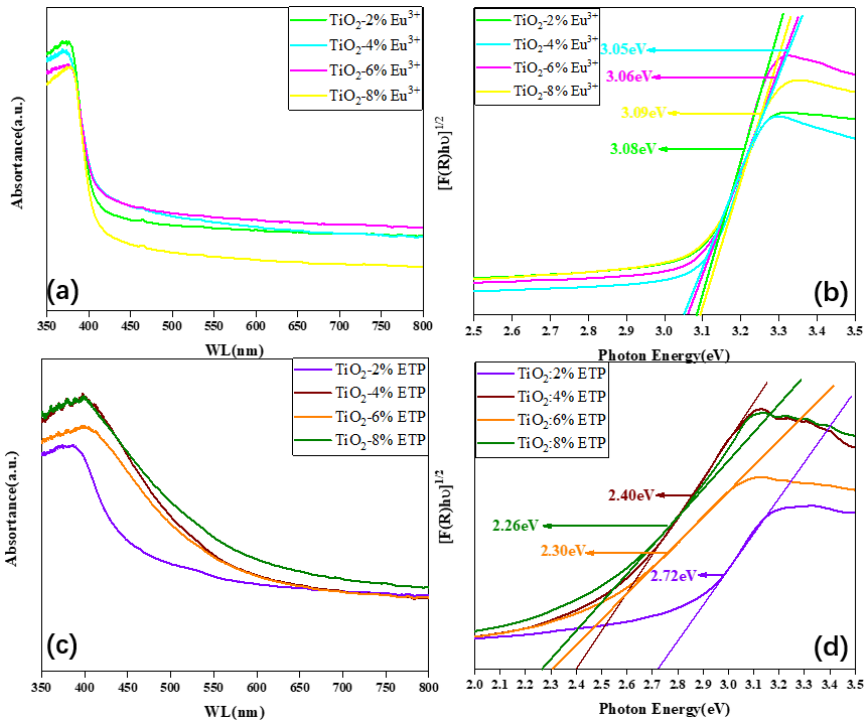


Fig. 7. UV-Vis spectra (a, c) of TiO_2-Eu^{3+} and TiO_2-ETP nanoparticles modified with variable concentration (2, 4, 6 and 8 %). Kubelka-Munk function for band gap estimation (b, d) of TiO_2-Eu^{3+} and TiO_2-ETP.

3.5 Photoluminescence analysis

The luminescence mechanism of Eu^{3+}-complexes is generally considered as

Deleted: After we studied the publications [31, 36, 50] on $Eu^{3+}$and its complexes-doped TiO_2, there were no informa about this interaction to be found.

Formatted: Highlight

Formatted: Font color: Red

Formatted: Font: Not Bold, Font color: Red, Complex Scr Font: Not Bold

Formatted: Font: Not Bold, Font color: Red, Complex Scr Font: Not Bold

Formatted: Font: Not Bold, Font color: Red, Complex Scr Font: Not Bold, Superscript

Formatted: Font: Not Bold, Font color: Red, Complex Scr Font: Not Bold

Formatted: Font: Not Bold, Font color: Red, Complex Scr Font: Not Bold, Subscript

Formatted: Font: Not Bold, Font color: Red, Complex Scr Font: Not Bold

Formatted: Font: Not Bold, Font color: Red, Complex Scr Font: Not Bold, Superscript

Formatted: Font: Not Bold, Font color: Red, Complex Scr Font: Not Bold

Formatted: Font: Times New Roman, Font color: Red

Formatted: Font: Not Bold, Font color: Red, Complex Scr Font: Not Bold

Formatted: Font color: Red, Subscript

Formatted: Font color: Red, Superscript

Formatted: Font color: Red, Not Highlight

Formatted: Font color: Red, Subscript, Not Highlight

Formatted: Font color: Red, Not Highlight

Deleted: (找合适的文献插入这里)

Formatted: Font color: Red, Not Highlight

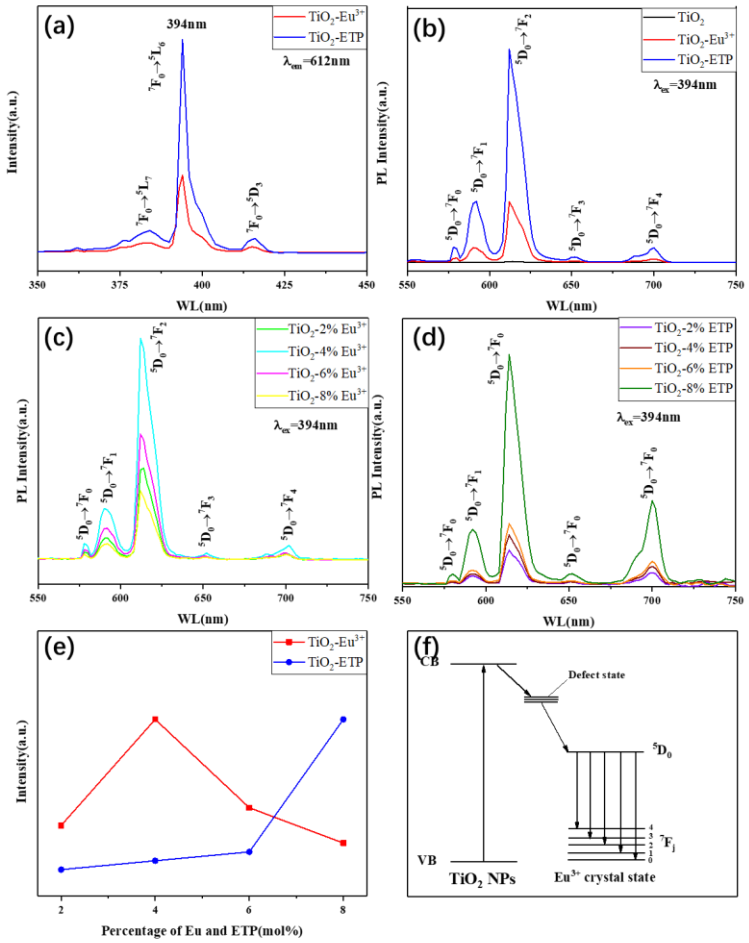
Deleted: , and thus cause the outer electron orbital hybrid between TiO_2 and Eu^{3+} or ETP [52]. Thus, the energy leve of conduction band and valence band of TiO_2 surely chang

Formatted: Font color: Red

Formatted: Font color: Red

Formatted: Font color: Red

follows: the organic ligand absorbs the external light energy, and thus, the electron transitions from the ground state to the excited singlet state. Normally, the excited electron will experience a intersystem transition from signglet to triplet. The triplet energy level matches the energy level S1 of Eu^{3+}, which makes the Eu^{3+} get the transferred energy to emit. The luminescence of TiO_2 is due to the electron transition between the valence band and the conduction band. Fig. 8(a) shows the excitation spectra of TiO_2-Eu^{3+} and TiO_2-ETP nanoparticles. The excitation spectrum is measured by the emission wavelength of the nanoparticles at 612 nm. The characteristic excitation peak is related to the 4f-4f transition of Eu^{3+} from $^7F_0$. It is seen that the excitation spectrum consists of sharp lines at 384, 394, 418, and 464 nm, which were assigned to the transitions $^7F_0 \rightarrow {}^5L_7$, $^7F_0 \rightarrow {}^5L_6$, $^7F_0 \rightarrow {}^5D_3$, and $^7F_0 \rightarrow {}^5D_2$ Eu^{3+} [55]. Strong peaks at 394 nm and 464 nm correspond to the $^7F_0 \rightarrow {}^5L_6$ and $^7F_0 \rightarrow {}^5D_2$ Eu^{3+} transitions. The intensity of the excitation spectrum of TiO_2-ETP is higher than that of Eu^{3+}. The organic ligands in ETP help absorb more ultraviolet light and convert it into energy. Fig. 8 (b) shows the emission spectra of TiO_2-Eu^{3+} and TiO_2-ETP. When excited at a wavelength of 394 nm, the emission spectrum consists of $^5D_0 \rightarrow {}^7F_J$ (J = 0, 1, 2, 3, 4) (578, 592, 612, 652, and 703 nm) Eu^{3+} transitions. Due to the allowable electric dipole of $^5D_0 \rightarrow {}^7F_2$ transition, the strongest red emission is produced, which is the largest at 612 nm. Fig. 8(c) is the emission spectrum with concentrations of Eu^{3+}:2, 4, 6, and 8 mol%. The influence of concentration on PL intensity is shown in Fig. 8(e). It can be seen that the optimal concentration of Eu^{3+} is 4 % [39]. When the concentration exceeds 4 %, the fluorescence of TiO_2-Eu^{3+} nanoparticles rapidly decrease. This means that 4%Eu^{3+} concentration is the up-solubility limit in TiO_2 host. However, the fluorescence intensity of TiO_2-ETP increases with increasing concentrations of ETP. This indicated that the organic ligands in ETP improve the solubility of ETP in TiO_2 host, which provide more effective "antenna effect" of organic ligands [56-58].



Deleted:

Fig. 8. The photoluminescence excitation spectra (a) and emission spectra (b, c, d) of TiO_2, TiO_2-Eu^{3+} and TiO_2-ETP nanoparticles; Fluorescence intensity vs. concentration curve (e) and Energy transfer diagram (f) of TiO_2, TiO_2-Eu^{3+} and TiO_2-ETP.

Deleted: (注意改这个 f 中的单线成多重线。改 e 中的 normorlzed intensity 为 Intensity.

Formatted: Highlight

Formatted: Highlight

Fig. 8 (f) shows a diagram of energy levels. Based on XRD, Raman and XPS analysis, Eu^{3+} and ETP were successfully modified on TiO_2 nanoparticle surfaces. In Fig. 8（f）, the phrase "defect state" is representative of a variety of defects. Europium ions will produce point defects in the crystal lattice and combine with oxygen atoms to form EU-O bonds[59], and the multiple defect energy levels were marked as multiple lines. Modification of Eu^{3+} and ETP can produce defects and these defects exists in the energy level. This indicates that the external ultraviolet rays are absorbed by the TiO_2 nanoparticles, and the energy enters the defect state. It is transferred to the Eu in the ETP, realizing the energy transfer process from TiO_2 to Eu. Because the energy level of the emission state of Eu^{3+} is lower than the energy level of the defect in TiO_2

nanoparticles, the energy is transferred from the defect state of titanium dioxide to the crystal field state of Eu^{3+} ions, which leads to effective photoluminescence of titanium dioxide nanoparticles. Due to the small size and a large number of nanoparticles, there are many surface states available for transferring energy to the states of the crystal field of Eu^{3+}. Fig. 9 shows the fluorescence lifetime diagram of TiO_2-Eu^{3+} and TiO_2-ETP. The fluorescence attenuation of TiO_2-ETP is slower than that of TiO_2-Eu^{3+}, and the quantum yield of TiO_2-ETP is higher than that of TiO_2-Eu^{3+}. The fluorescence lifetime of TiO_2-ETP and TiO_2-Eu^{3+} were 0.51ms and 0.39ms, and the quantum yields of TiO_2-ETP and TiO_2-Eu^{3+} were 10% and 5%.

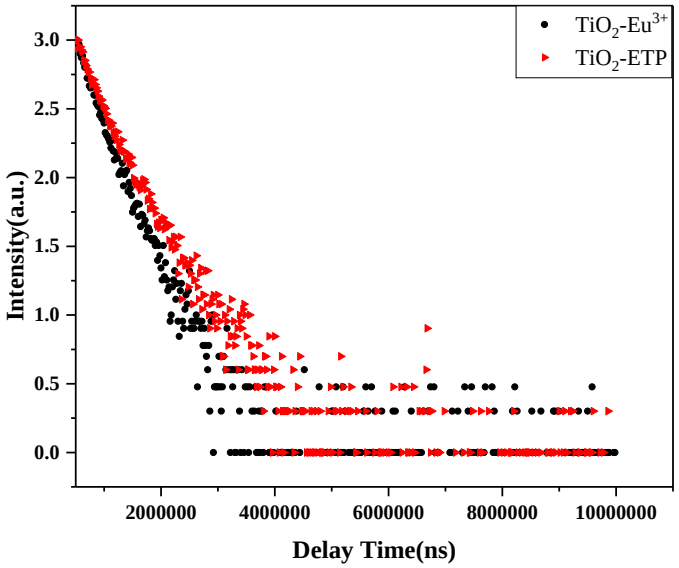


Fig. 9. the fluorescence lifetime diagram of TiO_2-Eu^{3+} and TiO_2-ETP.

3.6 Fluorescence spectra of TiO_2-ETP in the presence of metal ions

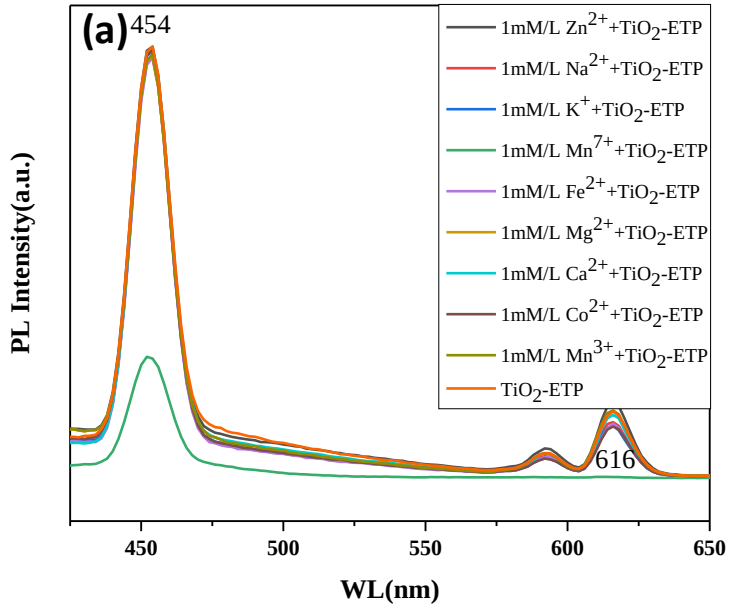
Eu^{3+} can be complexed with organic ligands containing oxygen or nitrogen groups, such as methyl 1H-benzotriazole and 1,10-phenanthroline monohydrate, and so on [60, 61]. Therefore, when the europium complex is in contact with metal ions, the fluorescence properties will change. In this paper, common metal cations such as Zn^{2+}, Mn^{3+}, K^{+}, Mn^{7+}, Fe^{2+}, Mg^{2+}, Ca^{2+}, and Co^{2+} are selected to explore whether these metal ions will affect the fluorescence properties of TiO_2-ETP. These experimental analyses prove that these common impurities will not affect the sensitivity of the sensor. In this work, the possible interfering ions have been tested in Fig. 10. On the other hand, for interfering molecules, we have previously reported the interfering data of organic molecules, such as carbohydrates, cholesterol, amino acids and etc., on the emission of Eu^{3+} complex in different hosts, and the results showed there are no quenching effect occurrence. [40][62].

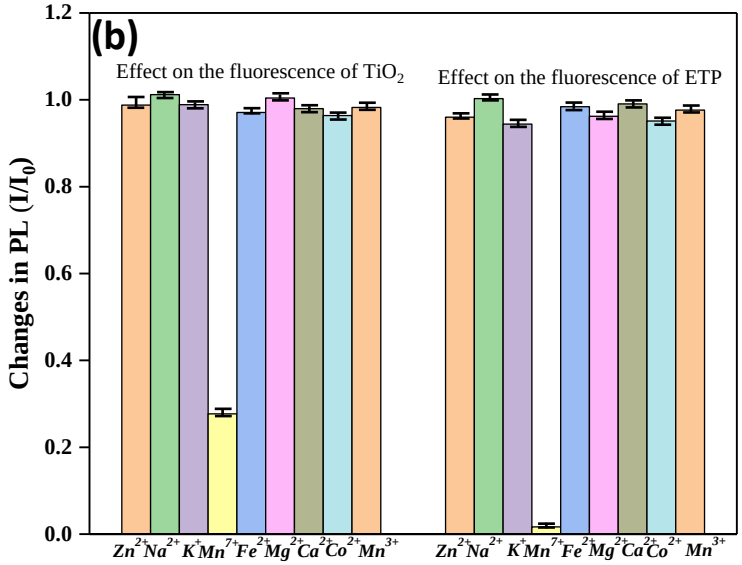
As shown in Fig. 10 (a), TiO_2-ETP shows a strong fluorescence peak located at 464 and 616 nm with excitation at λ_{ex} = 394 nm. The fluorescence of TiO_2-ETP is

influenced by the addition of Mn^{7+}, where a significant quenching effect can be observed. The fluorescence intensity of ETP-modified TiO_2 nanoparticles decreases with the increase of Mn^{7+} concentration in the solution. Fig. 10(b) shows the ratio (I / I_0) of the fluorescence intensity of TiO_2-ETP in an aqueous solution containing no metal ions and a solution containing a single metal ion. I_0 is the fluorescence intensity of TiO_2-ETP in the absence of metal ions at 464 nm and 616 nm, and I is the fluorescence intensity of TiO_2-ETP at 464 nm and 616 nm in the presence of a single metal ion. It can be seen from Fig. 10(b) that the addition of other metal ions except Mn^{7+} will not significantly reduce the fluorescence intensity of TiO_2-ETP. The aqueous solution containing Mn^{7+} will cause fluorescence quenching of TiO_2-ETP. TiO_2-ETP sensitive to Mn^{7+}. Then adding TiO_2-ETP to an aqueous solution containing a small amount of Mn^{7+}, the decrease in fluorescence intensity can also be detected. Experiments show that when other ions are present, only manganese will quench. The possible mechanism can suppose either the sharing light energy absorption of Mn^{7+} with ETP, or the excimer formation of $Mn^{7+}$with ETP. Therefore, the detection of Mn^{7+} content at the micromolar level can be achieved. Based on the different responses of TiO_2-ETP in the presence of Mn^{7+} and other metal ions, a method is proposed for determining the concentration of Mn^{7+}.

Fig. 10 (c, e) shows the relationship between the fluorescence intensity of TiO_2-ETP and the concentration of Mn^{7+} in an aqueous solution. For semiconductor TiO_2-ETP, fluorescence quenching is explained by the efficient electron transition process through annihilation of nonradiative electron-hole recombination. The weakening effect, i.e., quenching, normally is from the Mn^{7+} acceptance of energy from the excited states of TiO_2: ETP. Because there are two excited states corresponding to TiO_2 and ETP, the emissions of TiO_2 and ETP will be quenched by Mn^{7+}. The Stern-Volmer diagram used to determine the sensitivity of Mn^{7+} to TiO_2-ETP is shown in Fig. 10 (d, f, g). It can be observed that the Mn^{7+} concentration is linearly related to the fluorescence intensity. As the concentration of Mn^{7+} increases from 0 μmol/L to 1 mmol/L, the position of the fluorescence emission peak does not move, and the fluorescence intensity of TiO_2-ETP gradually decreases. This linear relationship means that the charge transfer mechanism between Mn^{7+} and TiO_2-ETP is caused by a dynamic mechanism. The inset to Fig. 10 (d) shows a graph of the variation of the radiation intensity (I / I_0) of TiO_2 at 464 nm as a function of the concentration of Mn^{7+}. Linear regression equation: $I / I_0 = 20.7C + 23570.9$ with a correlation coefficient R^2 equal to 0.99 (n = 14), where "I_0" is the TiO_2-ETP radiation intensity at 464 nm, "I" is the intensity of TiO_2-ETP with different concentration of Mn^{7+}, and "C" is the concentration of Mn^{7+}. Likewise, a graph of the variation of the emission intensity (I / I_0) of TiO_2-ETP at 616 nm as a function of the Mn^{7+} concentration is shown in the inset to Fig. 10 (f). The linear regression equation for Mn^{7+} is $I / I_0 = 13.8C + 2882.3$ ($R^2 = 0.98$, n = 14), respectively.

Deleted: Based on the weakening effect of TiO_2-ETP in th presence of Mn^{7+}, Fig. 10 (g) proposes a method for determining the concentration of Mn^{7+}.


(a)
454
616
1mM/L Zn2++TiO2-ETP
1mM/L Na2++TiO2-ETP
1mM/L K++TiO2-ETP
1mM/L Mn7++TiO2-ETP
1mM/L Fe2++TiO2-ETP
1mM/L Mg2++TiO2-ETP
1mM/L Ca2++TiO2-ETP
1mM/L Co2++TiO2-ETP
1mM/L Mn3++TiO2-ETP
TiO2-ETP
PL Intensity(a.u.)
450
500
550
600
650
WL(nm)


(b)
Effect on the fluorescence of TiO2
Effect on the fluorescence of ETP
Changes in PL (I/I0)
1.2
1.0
0.8
0.6
0.4
0.2
0.0
Zn2+ Na2+ K+ Mn7+ Fe2+ Mg2+ Ca2+ Co2+ Mn3+
Zn2+ Na2+ K+ Mn7+ Fe2+ Mg2+ Ca2+ Co2+ Mn3+

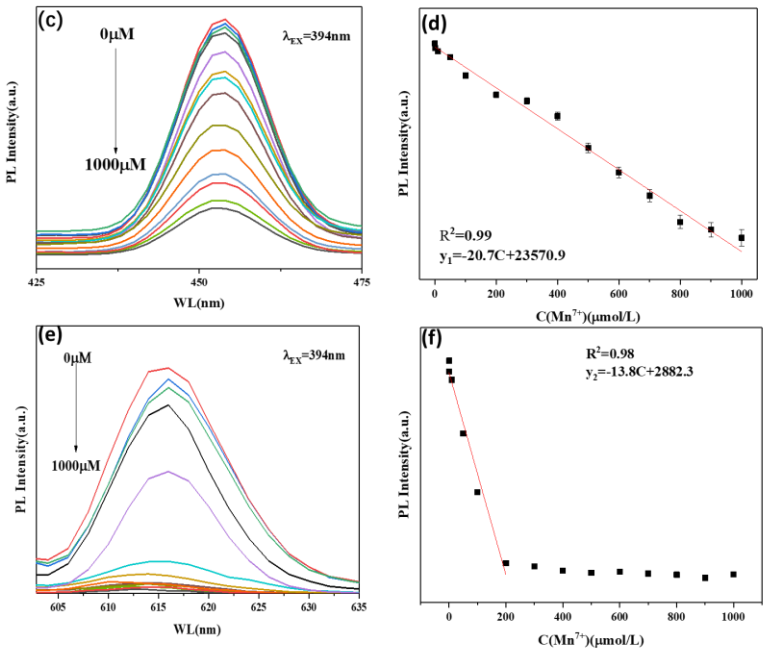


Fig. 10. (a) Fluorescence spectra of TiO_2-ETP with metal ions, (b) fluorescence intensity ratio (I/I_0) of the TiO_2-ETP in an aqueous solution containing no metal ions and a solution containing a single metal ion, (c,e) fluorescence intensity versus cation concentration for the addition of the Mn^{7+} ions, (d,f)the linear plot of $\Delta F/F_0$ against the concentration of Mn^{7+}.

4. Conclusions

In this study, we have synthesized TiO_2-ETP nanoparticles using a simple solvothermal process. XRD, Raman, and XPS patterns show that ETP is successfully embedded in TiO_2 nanoparticles. TiO_2-ETP nanoparticles exhibit a higher PL intensity than TiO_2-Eu^{3+} nanoparticles upon excitation at a wavelength of 394 nm. With the increase of Eu^{3+} concentration, the fluorescence intensity of TiO_2-Eu^{3+} at 550-750 nm increases, and the optimal concentration is 4.0 mol%. When the concentration of Eu^{3+} exceeds 4.0 mol%, the fluorescence decreases. TiO_2-ETP solves this problem and realizes that the intensity of fluorescence increases with increasing concentration. Aiming at the quenching effect of Mn^{7+} on the fluorescence intensity of TiO_2-ETP, a simple and efficient Mn^{7+} fluorescence sensor was proposed. Unlike the previously reported detection using Eu (TTA) $_3$phen or TiO_2, the detection range of nano-material TiO_2-ETP is larger, and the detection accuracy and sensitivity are higher. Experimental results show that the proposed new sensor is practical, can be used to detect real samples, has anti-interference ability, can be used for detection in complex environments, is simple to operate, and has more excellent application value.

Deleted:

Deleted: , (g)the linear plot of y_1/y_2 against the concentrat of Mn^{7+}.

Deleted: (在 d 和 f 中，已经有了拟合检出线，所以，可以去掉。避免审稿人再次提出来，耽误事); 重拍以下上面的图。

Formatted: Highlight

Formatted: Highlight

CRediT authorship contribution statement

Wenbin Yang: Data curation, Formal analysis, Writing - original draft, Writing - review & editing. Siqi Niu: Supervision. Yao Wang: Supervision. Linjun Huang: Supervision. Shichao Wang: Supervision. Ketul C. Popat: Conceptualization, Writing - review & editing. Matt J. Kipper: Writing - review & editing. Laurence A. Belfiore: Supervision. Jianguo Tang: Methodology, Conceptualization, Writing - review & editing, Funding acquisition.

Acknowledgement

This work was supported by (1) National Natural Science Foundation of China (51473082, 51878361); (2) State Key Project of International Cooperation Research (2016YFE0110800, 2017YFE0108300); (3) The National Program for Introducing Talents of Discipline to Universities ("111" plan); (4) 1st class discipline program of Materials Science of Shandong Province, and (5) The Double-Hundred Foreign Expert Program of Shandong Province.

References:

[1] S. Brown, N.L. Taylor, Could mitochondrial dysfunction play a role in manganese toxicity?, Environmental Toxicology & Pharmacology 7(1) (1999) 49-57.

[2] G.B. Gerber, A. Léonard, P. Hantson, Carcinogenicity, mutagenicity and teratogenicity of manganese compounds, Critical Reviews in Oncology & Hematology 42(1) (2002) 25-34.

[3] J. Crossgrove, Z. Wei, Manganese toxicity upon overexposure, Nmr in Biomedicine 17(8) (2004) 544-553.

[4] Q. Zhong, D.X. Liao, L.X. Ming, Review of Research in the Treatment of Electrolytic Manganese Waste water, China's Manganese Industry (2005).

[5] T. Horiguchi, Mechanism of Manganese Toxicity and Tolerance of Plants, Journal of Plant Nutrition 11(3) (1988) 235-246.

[6] T. Talasek, Ion Chromatography - ScienceDirect, Characterization of Integrated Circuit Packaging Materials 379(3) (1993) 240-242.

[7] M. Porento, V. Sutinen, T. Julku, R. Oikari, Detection of copper in water using on-line plasma-excited atomic absorption spectroscopy (AAS), Appl Spectrosc 65(6) (2011) 678-83.

[8] E.P. Nardi, F.S. Evangelista, L. Tormen, T.D. Saint′ Pierre, A.J. Curtius, S.S.D. Souza, F.B. Jr, The use of inductively coupled plasma mass spectrometry (ICP-MS) for the determination of toxic and essential elements in different types of food samples, Food Chemistry 112(3) (2009) 727-732.

[9] J.T. Groves, J. Lee, S.S. Marla, Detection and Characterization of an Oxomanganese(V) Porphyrin Complex by Rapid-Mixing Stopped-Flow Spectrophotometry, J.am.chem.soc 119(27) (1997) 6269-6273.

[10] D. Citak, M. Tuzen, M. Soylak, Speciation of Mn(II), Mn(VII) and total manganese in water and food samples by coprecipitation-atomic absorption spectrometry combination, J Hazard Mater 173(1-3) (2010) 773-7.

[11] A.X. Qian, G.H. He, X. Han, Separation and preconcentration of MnVII/MnII speciation on crosslinked chitosan and determination by flame atomic absorption spectrometry, Analyst 126(2) (2001) 239-41.

[12] Shashi, Pandya, Junhua, Yu, David, Parker, Engineering emissive europium and terbium complexes for molecular imaging and sensing, Dalton Transactions (2006).

[13] P.J. Potts, P.C. Webb, X-ray fluorescence spectrometry, Journal of Geochemical Exploration 44(1–3) (2012) 251–296.

[14] V.J. Ferreira, J.S. Almeida, V.A. Lemos, O.M.C. de Oliveira, K.S. Garcia, L.S.G. Teixeira, Determination of Cu, Ni, Mn, and Pb in diesel oil samples using reversed-phase vortex-assisted liquid-liquid microextraction associated with energy dispersive X-ray fluorescence spectrometry, Talanta 222 (2021) 121514.

[15] R.B. Thompson, Fluorescence Sensors and Biosensors, Fluorescence Sensors & Biosensors (2006).

[16] A.P.D. Silva, H.Q.N. Gunaratne, T. Gunnlaugsson, A.J.M. Huxley, T.E. Rice, ChemInform Abstract: Signaling Recognition Events with Fluorescent Sensors and Switches, Cheminform 28(44) (2010) no-no.

[17] P. Wu, X. Hou, J.J. Xu, H.Y. Chen, Ratiometric fluorescence, electrochemiluminescence, and photoelectrochemical chemo/biosensing based on semiconductor quantum dots, Nanoscale (2016) 10.1039.C6NR01912A.

[18] Y.R. Zhang, Z.M. Zhao, J.Y. Miao, B.X. Zhao, A ratiometric fluorescence probe based on a novel FRET platform for imaging endogenous HOCl in the living cells, Sensors & Actuators B Chemical 229 (2016) 408-413.

[19] S.M. A., Iftekhar, Uddin, Gwiy-Sang, Chung, A ratiometric fluorescent sensor for highly selective

detection of human carboxylesterase 2 and its application in living cells, Sensors & Actuators B Chemical (2014).
[20] L. Long, W. Lin, B. Chen, W. Gao, L. Yuan, Construction of a FRET-based ratiometric fluorescent thiol probe, Chemical communications (Cambridge, England) 47(3) (2010) 893.
[21] K. Wang, J. Qian, D. Jiang, Z. Yang, X. Du, K. Wang, Onsite naked eye determination of cysteine and homocysteine using quencher displacement-induced fluorescence recovery of the dual-emission hybrid probes with desired intensity ratio, Biosensors & Bioelectronics 65 (2015) 83-90.
[22] L.Y.K. Zhang, A novel core-satellite CdTe/Silica/Au \{NCs\} hybrid sphere as dual-emission ratiometric fluorescent probe for Cu2+, Biosensors and Bioelectronics (2014).
[23] F. Liu, J. He, M. Zeng, J. Hao, Q. Guo, Y. Song, L. Wang, Cu–hemin metal-organic frameworks with peroxidase-like activity as peroxidase mimics for colorimetric sensing of glucose, Journal of Nanoparticle Research 18(5) (2016) 1-9.
[24] Dual-Emission of Lanthanide Metal–Organic Frameworks Encapsulating Carbon-Based Dots for Ratiometric Detection of Water in Organic Solvents, Analytical Chemistry 88(3) (2016) 1748.
[25] Z. Zhang, Y. Zhao, Q. Gong, Z. Li, J. Li, MOFs for CO2 capture and separation from flue gas mixtures: the effect of multifunctional sites on their adsorption capacity and selectivity, Chemical Communications 49(7) (2012) 653-661.
[26] Y. Cui, Y. Yue, G. Qian, B. Chen, Luminescent Functional Metal-Organic Frameworks, Chemical Reviews 112(2) (2012) 1126-1162.
[27] Rocha, J., Carlos, L., Paz, F., A., Ananias, D., Luminescent multifunctional lanthanides-based metal-organic frameworks, Chemical Society Reviews (2011).
[28] Y. Zhou, D. Zhang, J. Zeng, N. Gan, J. Cuan, A luminescent Lanthanide-free MOF nanohybrid for highly sensitive ratiometric temperature sensing in physiological range, Talanta 181 (2018) 410-415.
[29] A.M. Kaczmarek, V.H. Kristof, V.D. Rik, Enhanced luminescence in Ln3?-doped Y?WO? (Sm, Eu, Dy) 3D microstructures through Gd3? codoping, Inorganic Chemistry 53(18) (2014) 9498-508.
[30] Dorenbos, P., The 4fn4fn-15d transitions of the trivalent lanthanides in halogenides and chalcogenides, Journal of Luminescence (2000).
[31] M.H.V. Werts, R.T.F. Jukes, J.W. Verhoeven, The emission spectrum and the radiative lifetime of Eu3+ in luminescent lanthanide complexes, Physical Chemistry Chemical Physics 4(9) (2002) 1542-1548.
[32] A.L. Linsebigler, G. Lu, J.T. Yates, Photocatalysis on TiO2 Surfaces: Principles, Mechanisms, and Selected Results, Chemical Reviews 95(3) (1995) 735-758.
[33] D. Zhai, K. Zhang, Z. Yong, H. Sun, G. Fan, Mesoporous silica equipped with europium-based chemosensor for mercury ion detection: Synthesis, characterization, and sensing performance, Inorganica Chimica Acta 387(none) (2012) 396-400.
[34] M. Zhang, G. Zhan, Z. Chen, Iodometric Amplification Method for the Determinations of Microgram Amounts of Manganese(II), Manganese(VII), Chromium(III) and Chromium(VI) in Aqueous Solution, Analytical ences 14(6) (2005) 1077-1083.
[35] K. Zheng, X. Xu, H. Zhao, Y. Song, Y. Sheng, Q. Huo, H. Zou], Facile synthesis of TiO2:Eu3+ spindle shaped nanoparticles from titanate nanobelt precursors, Powder Technology (2012).
[36] M. Lazzeri, A. Vittadini, A. Selloni, Erratum, Structure and energetics of stoichiometric TiO2 anatase surfaces, Physical Review B (2001).
[37] H. Wang, Y. Wang, Y. Yang, X. Li, C. Wang, Photoluminescence properties of the rare-earth ions in the TiO2 host nanofibers prepared via electrospinning, Materials Research Bulletin 44(2) (2009) 408-414.

[38] M. Vranješ, J. Kuljanin-Jakovljević, T. Radetić, M. Stoiljković, M. Mitrić, Z.V. Šaponjić, J. Nedeljković, Structure and luminescence properties of Eu3+ doped TiO2 nanocrystals and prolate nanospheroids synthesized by the hydrothermal processing, Ceramics International 38(7) (2012) 5629-5636.
[39] X. Qi, H. Zou, Y. Song, H. Zhang, H. Zhao, Z. Shi, Y. Sheng, Hydrothermal synthesis and luminescence properties of TiO2: Eu3+ submicrospheres, Ceramics International 40(8) (2014) 12993-12997.
[40] R.C. Hsiao, N.S. Arul, D. Mangalaraj, R.S. Juang, Influence of Eu3+ doping on the degradation property of TiO2 nanostructures, Journal of Optoelectronics & Advanced Materials 12(2) (2010) 193-198.
[41] M. Pal, U. Pal, J.M.G.Y. Jiménez, F. Pérez-Rodríguez, Effects of crystallization and dopant concentration on the emission behavior of TiO2:Eu nanophosphors, Nanoscale Research Letters 7(1) (2012) 1-1.
[42] W.F. Zhang, Y.L. He, M.S. Zhang, Z. Yin, Q.Y.Z. Chen, Raman scattering study on anatase TiO2 nanocrystals, Journal of Physics D Applied Physics 33(8) (2000) 912.
[43] J. Zhang, M. Li, Z. Feng, J. Chen, C. Li, UV Raman spectroscopic study on TiO2. I. Phase transformation at the surface and in the bulk, Journal of Physical Chemistry B 110(2) (2006) 927-935.
[44] D. Bersani, P.P. Lottici, X.Z. Ding, Phonon confinement effects in the Raman scattering by TiO2 nanocrystals, Applied Physics Letters 72(1) (1998) 73-75.
[45] B. Su, S. Wang, W. Yang, Y. Wang, L. Huang, K.C. Popat, M.J. Kipper, L.A. Belfiore, J. Tang, Synthesis of Eu-modified luminescent Titania nanotube arrays and effect of voltage on morphological, structural and spectroscopic properties, Materials Science in Semiconductor Processing 113 (2020).
[46] X. Tan, Q. Fan, X. Wang, B. Grambow, Eu(III) sorption to TiO2 (anatase and rutile): batch, XPS, and EXAFS studies, Environmental ence & Technology 43(9) (2009) 3115-21.
[47] X. Tan, Q. Fan, X. Wang, B. Grambow, Eu(III) sorption to TiO2 (anatase and rutile): batch, XPS, and EXAFS studies, Environmental Science & Technology 43(9) (2009) 3115-21.
[48] X. Feng, L. Yang, N. Zhang, Y. Liu, A facile one-pot hydrothermal method to prepare europium-doped titania hollow phosphors and their sensitized luminescence properties, Journal of Alloys and Compounds 506(2) (2010) 728-733.
[49] S.B. Khan, M.M. Rahman, A.M. Asiri, H.M. Marwani, S.M. Bawaked, K.A. Alamry, Co3O4 co-doped TiO2 nanoparticles as a selective marker of lead in aqueous solution, New Journal of Chemistry 37 (2013).
[50] J. Yu, Q. Xiang, M. Zhou, Preparation, characterization and visible-light-driven photocatalytic activity of Fe-doped titania nanorods and first-principles study for electronic structures, Applied Catalysis B: Environmental 90(3-4) (2009) 595-602.
[51] V.N. Krasila??Nikov, V.P. Zhukov, L.A. Perelyaeva, I.V. Baklanova, I.R. Shein, Electronic band structure, optical absorption, and photocatalytic activity of iron-doped anatase, Physics of the Solid State 55(9) (2013) 1903-1912.
[52] H. Yamashita, M. Harada, J. Misaka, M. Takeuchi, M. Anpo, Degradation of propanol diluted in water under visible light irradiation using metal ion-implanted titanium dioxide photocatalysts, Journal of Photochemistry & Photobiology A Chemistry 148(1-3) (2002) 257-261.
[53] D. Komaraiah, E. Radha, N. Kalarikkal, J. Sivakumar, M.R. Reddy, R. Sayanna, Structural, optical and photoluminescence studies of sol-gel synthesized pure and iron doped TiO2 photocatalysts, Ceramics International (2019).
[54] D. Singh, N. Singh, S.D. Sharma, C. Kant, C.P. Sharma, R.R. Pandey, K.K. Saini, Bandgap modification of TiO2 sol–gel films by Fe and Ni doping, Journal of Sol-Gel Science and Technology 58(1) (2011) 269-

276.
[55] X. Qi, Y. Song, Y. Sheng, H. Zhang, H. Zhao, Z. Shi, H. Zou, Controllable synthesis and luminescence properties of TiO2:Eu3+ nanorods, nanoparticles and submicrospheres by hydrothermal method, Optical Materials 38 (2014) 193-197.
[56] P.K. Shahi, A.K. Singh, S.K. Singh, S.B. Rai, B. Ullrich, Revelation of the Technological Versatility of the Eu(TTA)3Phen Complex by Demonstrating Energy Harvesting, Ultraviolet Light Detection, Temperature Sensing, and Laser Applications, Acs Appl Mater Interfaces (2015) 18231-18239.
[57] B. Yan, Y. Li, Luminescent ternary inorganic-organic mesoporous hybrids Eu(TTASi-SBA-15)phen: covalent linkage in TTA directly functionalized SBA-15, Dalton Trans 39(6) (2010) 1480-1487.
[58] Mustafa, Burak, Coban, Cagdas, Kocak, Hulya, Kara, Muhittin, Aygun, Asma, Magnetic properties and sensitized visible and NIR luminescence of DyIII and EuIII coordination polymers by energy transfer antenna ligands, Molecular Crystals and Liquid Crystals 648(1) (2017) 202-215.
[59] K.L. Frindell, M.H. Bartl, M.R. Robinson, G.C. Bazan, A. Popitsch, G.D. Stucky, Visible and near-IR luminescence via energy transfer in rare earth doped mesoporous titania thin films with nanocrystalline walls, Journal of Solid State Chemistry 172(1) (2003) 81-88.
[60] A.A. Knyazev, M.E. Karyakin, A.S. Krupin, K.A. Romanova, Y.G. Galyametdinov, Influence of Eu(III) Complexes Structural Anisotropy on Luminescence of Doped Conjugated Polymer Blends, Inorganic Chemistry 56(11) (2017).
[61] L. Rino, W. Simes, G. Santos, F.J. Fonseca, A.M. Andrade, V.A.F. Deichmann, L. Akcelrud, L. Pereira, Photo and electroluminescence behavior of Tb(ACAC)3phen complex used as emissive layer on organic light emitting diodes, Journal of Non-Crystalline Solids 354(47-51) (2008) 5326-5327.
[62] Z. Song, J. Wang, J. Liu, X. Wang, J. Tang, Eu3+-Induced Polysaccharide Nano-Dumbbell Aggregates (PNDA) as Drug Carriers to Smartly Report Drug Concentration through Variable Fluorescence, Sensors and Actuators B Chemical 336(10) (2021) 129724.